Heat Kernel Smoothing of Anatomical Manifolds via Laplace-Beltrami Eigenfunctions

Department of Biostatistics and Medical Informatics

University of Wisconsin-Madison

Technical Report 211

Seongho Seo[1], Moo K. Chung[1,2], Houri K. Vorperian[3]
[1] Department of Brain and Cognitive Sciences
Seoul National University, Korea
dansoc@snu.ac.kr
[2] Department of Biostatistics and Medical Informatics
Waisman Laboratory for Brain Imaging and Behavior
mkchung@wisc.edu
[3] Vocal Tract Development Laboratory, Waisman Center
University of Wisconsin, Madison, WI 53706, USA
vorperian@waisman.wisc.edu

June 12, 2010

Abstract

We present a novel surface smoothing framework using the Laplace-Beltrami eigenfunctions. The Green's function of an isotropic diffusion equation on a manifold is analytically represented using the eigenfunctions of the Laplace-Beltraimi operator. The Green's function is then used in explicitly constructing heat kernel smoothing as a series expansion of the eigenfunctions. Unlike many previous surface diffusion approaches, diffusion is analytically represented using the eigenfunctions reducing numerical inaccuracy. Our numerical implementation is validated against the spherical harmonic representation of heat kernel smoothing on a unit sphere. The proposed framework is illustrated with mandible surfaces, and is compared to a widely used iterative kernel smoothing method in computational anatomy. The MATLAB source code is freely available at `http://brainimaging.waisman.wisc.edu/~chung/lb`

Keywords: heat kernel, Laplace-Beltrami operator, mandible, surface diffusion.

1 Introduction

In medical image analysis, anatomical surfaces obtained from MRI and CT are often represented as triangular meshes. Image segmentation and surface extraction process themselves are likely to introduce noise to the mesh coordinates. It is imperative to reduce the mesh noise while preserving the geometric details of the objects for various applications.

Diffusion equations have been widely used in image processing as a form of noise reduction starting with Perona and Malik in 1990 [1]. Motivated by Perona and Malik's work, many methods have been proposed to smooth out surface data based on diffusion [2, 3, 4]. Although numerous efforts have been devised for surface fairing and mesh regularization [5, 6, 7, 8], a few have also tried to smooth out measurements defined on surfaces for the purpose of statistical analysis [2, 9, 10, 11, 12]. Iterated kernel smoothing has been also a widely used method in approximately solving diffusion equations on surfaces [12, 13, 14].

Particularly in brain imaging, isotropic heat diffusion on surfaces was introduced for subsequent statistical analysis involving the random field theory that assumes an isotropic covariance function as a noise model [2, 3, 9, 10, 11]. Since then, isotropic diffusion has been mainly used as the standard smoothing technique. Such approaches mainly use finite element or finite difference schemes which is known to suffer numerical instability if the forward Euler scheme is used. Instead of directly solving diffusion, iterated kernel smoothing is often used in smoothing various cortical surface data: cortical curvatures [15, 16], cortical thickness [17, 18], hippocampus [19, 20], magnetoencephalography (MEG) [21] and functional-MRI [22, 23]. In iterated kernel smoothing, kernel weights are spatially adapted to follow the shape of the heat kernel in a discrete fashion along a manifold. In the tangent space of the manifold, the heat kernel can be approximated linearly using the Gaussian kernel for small bandwidth. A kernel with large bandwidth is then constructed iteratively applying the kernel with small bandwidth. However, this process compounds the linearization error at each iteration as we will demonstrate in the paper.

In this paper, we propose a new smoothing framework that constructs the heat kernel analytically using the eigenfunctions of the Laplace-Beltrami operator, avoiding the need for the linear approximation [12, 13, 14]. Although solving for the eigenfunctions of the Laplace-Beltrami operator requires the finite element method, the proposed method is analytic in a sense that heat kernel smoothing is formulated as a series expansion explicitly. We are not claiming our whole framework to be analytic which is theoretically impossible when we deal with real data. The proposed method represents isotropic heat diffusion analytically as a series expansion so it avoids the numerical instability associated with solving the diffusion equations numerically using the forward Euler scheme [2, 9, 10]. Our radically different framework can bypass various numerical problems associated with previous approaches: numerical instability, slow convergence, and accumulated linearization error. Although there are many papers on solving diffusion equations on arbitrary triangular meshes [2, 3, 4, 24], this is the first paper that explicitly and correctly constructs heat kernel for an arbitrary surface and solved heat diffusion using the eigenfunctions of Laplace-Beltrami operator.

The proposed method is illustrated with triangulated mandible surfaces obtained from CT scans and validated on a uniformly sampled spherical mesh.

2 Heat Kernel Smoothing

Consider a real-valued measure Y defined on a closed compact manifold $\mathcal{M} \subset \mathbb{R}^3$. We assume the following additive model on Y:

$$Y(p) = \theta(p) + \epsilon(p), \tag{1}$$

where $\theta(p)$ is the unknown mean signal to be estimated and $\epsilon(p)$ is a zero-mean Gaussian random field. We may assume further $Y \in L^2(\mathcal{M})$, the space of square integrable functions on $\mathcal{M}$ with the inner product

$$\langle f, g \rangle = \int_{\mathcal{M}} f(p)g(p)\, d\mu(p), \tag{2}$$

where μ is the Lebesgue measure such that $\mu(\mathcal{M})$ is the total area or volume of $\mathcal{M}$. Solving

$$\Delta\psi_j = -\lambda\psi_j, \tag{3}$$

for the Laplace-Beltrami operator Δ on $\mathcal{M}$, we order eigenvalues

$$0 = \lambda_0 < \lambda_1 \leq \lambda_2 \leq \cdots,$$

and corresponding eigenfunctions $\psi_0, \psi_1, \psi_2, \cdots$ [13, 25, 26]. Then, the eigenfunctions ψ_j form an orthonormal basis in $L^2(\mathcal{M})$ [13, 25, 27].

Using the eigenfunctions, *heat kernel* $K_\sigma(p, q)$ is then analytically defined as

$$K_\sigma(p, q) = \sum_{j=0}^{\infty} e^{-\lambda_j \sigma} \psi_j(p) \psi_j(q), \tag{4}$$

where σ is the bandwidth of the kernel. Then *heat kernel smoothing* of Y is defined analytically as

$$K_\sigma * Y(p) = \sum_{j=0}^{\infty} e^{-\lambda_j \sigma} \beta_j \psi_j(p), \tag{5}$$

where $\beta_j = \langle Y, \psi_j \rangle$ are Fourier coefficients [12, 13]. This is taken as the estimate for the unknown mean signal θ.

The heat kernel (4) is the Green's function, or the fundamental solution, of the isotropic heat diffusion equation

$$\frac{\partial f}{\partial \sigma} = \Delta f. \tag{6}$$

Therefore, the heat kernel smoothing (5) is also the solution to the diffusion equation (6) with the initial condition $f(p, \sigma = 0) = Y(p)$ after time σ. Unlike all previous approaches to heat diffusion [2, 3, 4, 24], our formulation avoids the direct numerical discretization of the underlying diffusion equations. Instead we are discretizing the basis functions of the given manifold $\mathcal{M}$ where the diffusion equations are defined.

In this new framework, we need to compute the terms in (5). We first solve for the eigensystem (3) and obtain λ_j and ψ_j (section 3.1). The Fourier coefficients β_j are estimated using the iterative residual fitting (IRF) algorithm (section 3.2). The finite expansion of (5) is then used as the finite estimate for the underlying signal θ in (1). The degree for truncating the infinite series is automatically determined using the forward model selection procedure (section 3.2). The numerical accuracy of the whole framework is validated on a unit sphere where the mathematical ground truth is known in terms of spherical harmonics (section 4.3). Taking our framework as the baseline, we have compared our proposed method to iterated kernel smoothing (section 4.4) to show the improvement of our method to the previous approach.

3 Numerical Implementation

3.1 Generalized Eigenvalue Problem.

Since the closed form expression for the eigenfunctions of the Laplace-Beltrami operator on an arbitrary surface is unknown, the eigenfunctions are numerically computed by discretizing the Laplace-Beltrami operator. To solve the eigensystem (3), we need to discretize it on a triangular mesh using the Cotan formulation [3, 26, 28, 29]. In a related work, Qiu et al. [29] presented a similar Cotan discretization of the eigensystem and used to construct splines on a manifold; however, there is no direct mathematical relation between splines and heat kernel smoothing. We briefly review the Cortan formulation for discretizating the eigensystem.

Let N_T be the number of triangles in the mesh that approximates the underlying manifold $\mathcal{M}$. We seek a piecewise differentiable solution f_i in the i-th triangle T_i such that the solution $f_i(x)$ is continuous across neighboring triangles. The solution f for the whole mesh is then

$$f(x) = \sum_{i=1}^{N_T} f_i(x).$$

Let $p_{i_1}, p_{i_2}, p_{i_3}$ be the vertices of element T_i. In T_i, we estimate f_i linearly as

$$f_i(x) = \sum_{k=1}^{3} \xi_{i_k} f(p_{i_k}),$$

where nonnegative ξ_{i_k} are given by the *barycentric coordinates* [3, 7]. Any point $x \in T_i$ is uniquely determined by two conditions:

$$x = \sum_{k=1}^{3} \xi_{i_k}(x) p_{i_k}, \ \sum_{k=1}^{3} \xi_{i_k}(x) = 1.$$

Let g be an arbitrary piecewise linear function given by

$$g(x) = \sum_{i=1}^{N_T} \sum_{k=1}^{3} \xi_{i_k}(x) g_{i_k},$$

where $g_{i_k} = g(p_{i_k})$ are the values of function g evaluated at vertices p_{i_k} of T_i. For the function f, we can represent similarly as $f_{i_k} = f(p_{i_k})$. Since the Laplace-Beltrami operator is *self-adjoint*, we have

$$\int g \Delta f \, d\mu = -\int \langle \nabla f, \nabla g \rangle \, d\mu = \int f \Delta g \, d\mu.$$

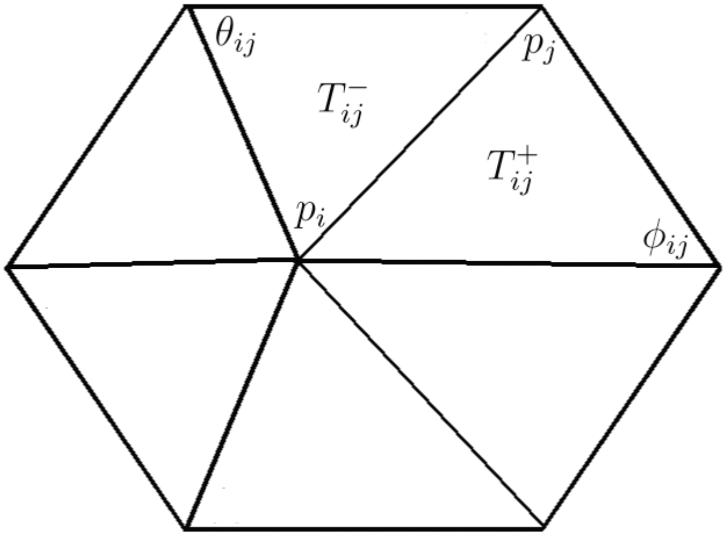

Figure 1: A typical 1-ring neighbor of a mesh vertex p_i. θ_{ij} and ϕ_{ij} are the angles opposite to the edge p_ip_j. T_{ij}^- and T_{ij}^+ are triangles sharing the edge p_ip_j.

Then the integral version of the eigensystem $\Delta f = -\lambda f$ in the triangle T_i can be written as

$$\int_{T_i} g\lambda f \, d\mu = \int_{T_i} \langle \nabla f, \nabla g \rangle \, d\mu. \tag{7}$$

The left-hand term in (7) can be written further as

$$\int_{T_i} g\lambda f \, d\mu = \sum_{k,l=1}^{3} g_{i_k} \lambda f_{i_l} \int_{T_i} \xi_{i_k} \xi_{i_l} \, d\mu \tag{8}$$

$$= \lambda \mathbf{G}_i' \mathbf{A}^i \mathbf{F}_i, \tag{9}$$

where $\mathbf{G}_i = (g_{i_1}, g_{i_2}, g_{i_3})', \mathbf{F}_i = (f_{i_1}, f_{i_2}, f_{i_3})'$ and 3×3 mass matrix

$$\mathbf{A}^i = (A_{kl}^i), \; A_{kl}^i = \int_{T_i} \xi_{i_k} \xi_{i_l} \, d\mu.$$

It can be shown that

$$\mathbf{A}^i = \frac{|T_i|}{12} \begin{pmatrix} 2 & 1 & 1 \\ 1 & 2 & 1 \\ 1 & 1 & 2 \end{pmatrix},$$

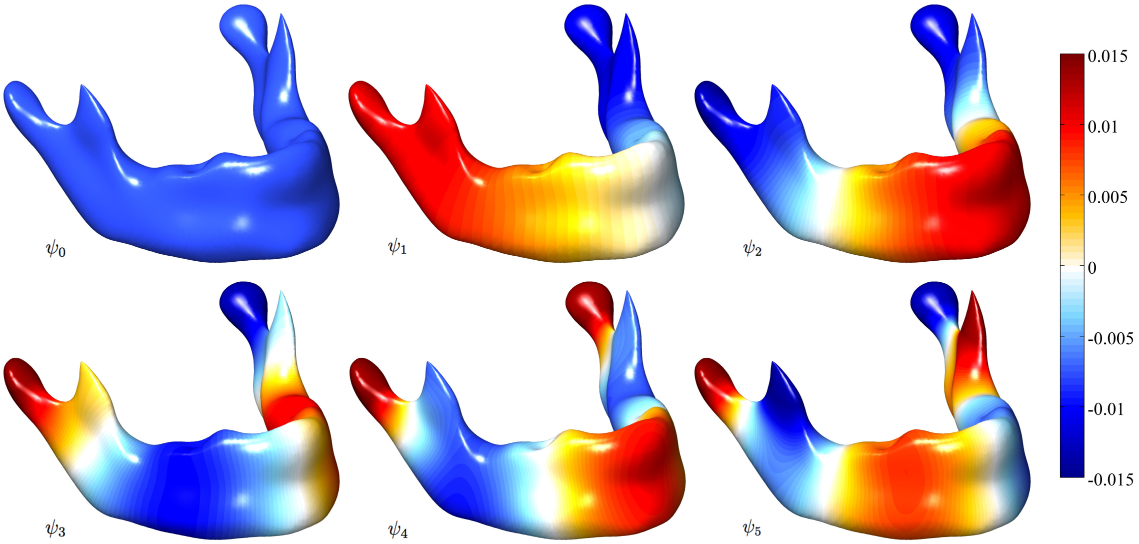

Figure 2: Eigenfunctions of various degrees for a sample mandible surface. The eigenfunctions are projected on the surface smoothed by the proposed heat kernel smoothing with $\sigma = 0.5$ and degree $k = 132$. The first eigenfunction is simply $\psi_0 = 1/\sqrt{\mu(\mathcal{M})}$. The color scale is thresholded at ± 0.015 for better visualization.

where $|T_i|$ is the area of the triangle T_i [30, 31]. Similarly, the right-hand term in (7) is

$$\int_{T_i} \langle \nabla f, \nabla g \rangle \, d\mu = \sum_{k,l=1}^{3} g_{i_k} f_{i_l} \int_{T_i} \langle \nabla \xi_{i_k}, \nabla \xi_{i_l} \rangle \, d\mu \tag{10}$$

$$= \mathbf{G}_i' \mathbf{C}^i \mathbf{F}_i, \tag{11}$$

where 3×3 matrix $\mathbf{C}^i$ is given by

$$\mathbf{C}^i = (C^i_{kl}), \; C^i_{kl} = \int_{T_i} \langle \nabla \xi_{i_k}, \nabla \xi_{i_l} \rangle \, d\mu.$$

Since T_i is planar, the gradient $\nabla \xi_{i_k}$ is the standard planar gradient. The matrix $\mathbf{C}^i$ can be further written as [30, 31, 32]

$$\frac{1}{2} \begin{pmatrix} \cot\theta_{i_2} + \cot\theta_{i_3} & -\cot\theta_{i_3} & -\cot\theta_{i_2} \\ -\cot\theta_{i_3} & \cot\theta_{i_1} + \cot\theta_{i_3} & -\cot\theta_{i_1} \\ -\cot\theta_{i_2} & -\cot\theta_{i_1} & \cot\theta_{i_1} + \cot\theta_{i_2} \end{pmatrix},$$

where θ_{i_k} is the incident angle of vertex p_{i_k} in triangle T_i. By equating (9) and (11), we obtain

$$\mathbf{A}^i \lambda \mathbf{F}_i = \mathbf{C}^i \mathbf{F}_i. \tag{12}$$

We solve (12) by assembling all triangles. To simplify the indexing, we will use slightly different notations from now on. Let $N(p_i)$ be the set of neighboring vertices around p_i, and let $T_{ij}^-$and T_{ij}^+ denote two triangles sharing vertices p_i, and p_j. Let two angles opposite to the edge containing p_i and p_j be ϕ_{ij} and θ_{ij} respectively for T_{ij}^+ and T_{ij}^- (Fig. 1). Then, the assembled sparse matrices $\mathbf{A} = (A_{ij})$ is computed as follows. The diagonal entries are

$$A_{ii} = \frac{1}{12} \sum_{p_j \in N(p_i)} (T_{ij}^+ + T_{ij}^-),$$

and the off-diagonal entries are

$$A_{ij} = \frac{1}{12}(T_{ij}^+ + T_{ij}^-),$$

if p_i and p_j are adjacent, and $A_{ij} = 0$ otherwise. The global coefficient matrix $\mathbf{C} = (C_{ij})$, which is the assemblage of individual element coefficients is given similarly using the cotan formulation. The diagonal entries are

$$C_{ii} = \frac{1}{2} \sum_{p_j \in N(p_i)} (\cot \theta_{ij} + \cot \phi_{ij}),$$

and the off diagonal entries are

$$C_{ij} = -\frac{1}{2}(\cot \theta_{ij} + \cot \phi_{ij}),$$

if p_i and p_j are adjacent, and $C_{ij} = 0$ otherwise. When we construct $\mathbf{A}$ and $\mathbf{C}$ matrices, we compute the off-diagonal elements first and the diagonal elements next by summing the off-diagonal terms in the first ring neighbors. Finally, we can obtain the following generalized eigenvalue problem:

$$\mathbf{C}\psi = \lambda \mathbf{A} \psi. \tag{13}$$

Since $\mathbf{C}$ and $\mathbf{A}$ are large sparse matrices, we have solved (13) using the *Implicitly Restarted Arnoldi Method* [33, 34] without consuming large amount of memory and time for sparse entries. The `MATLAB` code is given at `http://brainimaging.waisman.wisc.edu/~chung/lb`.

Fig. 2 shows the first few eigenfunctions for a mandible surface. The first eigenfunction is trivially given as $\psi_0 = 1/\sqrt{\mu(\mathcal{M})}$ and $\lambda_0 = 0$ for a closed compact surface. It is possible to have multiple eigenfunctions corresponding to a single eigenvalue. The multiplicity of the eigenvalues of the Laplace-Beltrami operator is known although the exact number of multiplicity is unknown for arbitrary manifolds [35]. For smooth genus zero surfaces, the multiplicity m is bounded by

$$m(\lambda_k) \leq 2k - 3 \text{ for } k \geq 2.$$

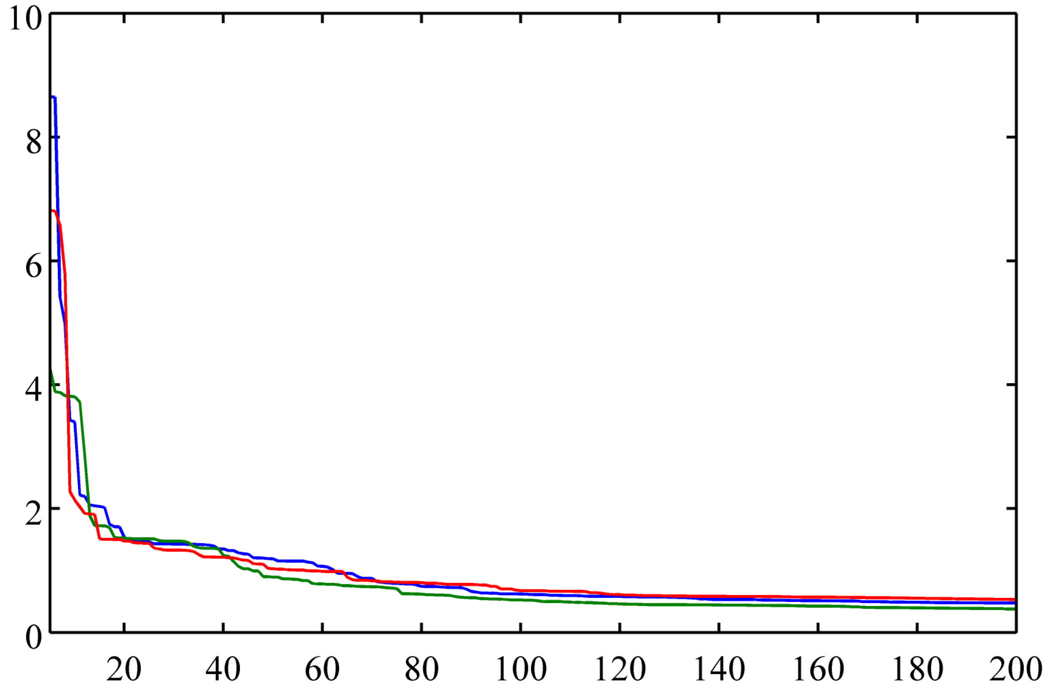

Figure 3: The plot of the root mean squared errors (RMSE) for coordinates x (blue), y (red) and z (green) for a mandible surface, varying degree k from 5 to 200. The optimal degree for the surface is 132 for bandwidth $\sigma = 0.5$.

Suppose $\psi_{k1}, \cdots \psi_{kk_m}$ are k_m eigenfunctions corresponding to eigenvalue λ_k. Then any linear combination of ψ_{kj} is also an eigenfunction. Hence, within the same degree, the space of eigenfunctions form a vector space. The eigenfunctions form a complete orhonormal basis in the space of square integrable functions, $L^2(\mathcal{M})$, so all other possible orthonormal basis is a linear combination of eigenfunctions.

3.2 Iterative Residual Fitting Algorithm.

Once we obtain the eigenfunctions numerically, we construct the subspace $\mathcal{H}_k$, which is spanned by up to k-th degree basis. Then we approximate the functional data Y in $\mathcal{H}_k$ by minimizing the sum of squared residual:

$$\arg\min_{f \in \mathcal{H}_k} \|f - Y\|^2 = \sum_{j=0}^{k} \beta_j \psi_j(p), \tag{14}$$

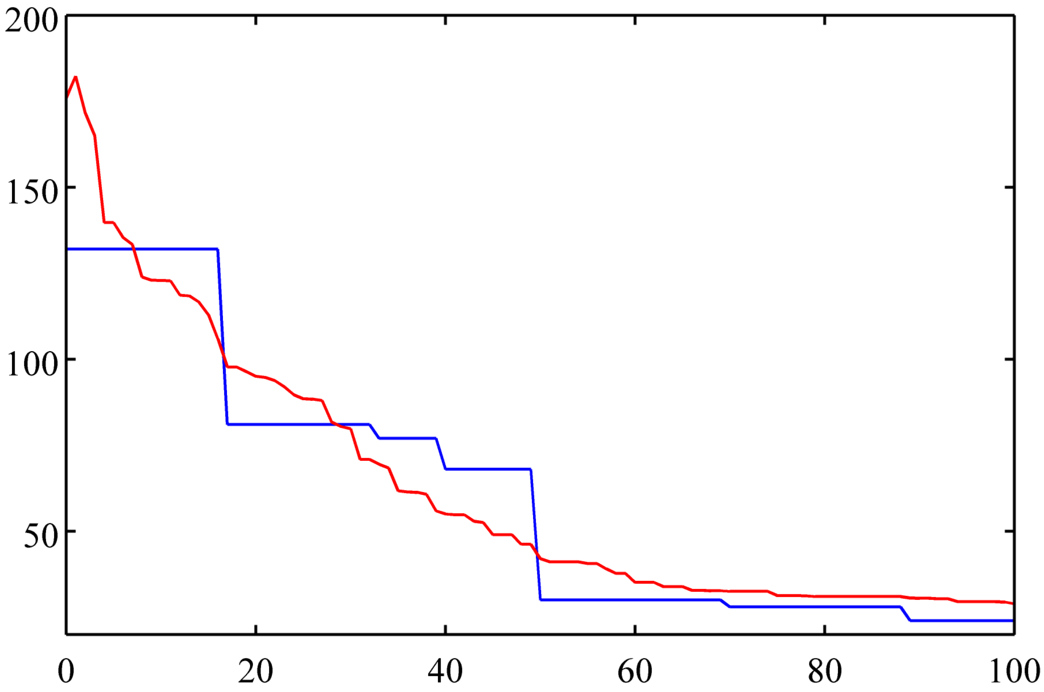

Figure 4: The plot of optimal degree (vertical) over varying bandwidths ($0 \leq \sigma \leq 100$) for a mandible surface (blue) and the average optimal degree for 10 mandible surfaces (red). As smoothing increases, the optimal degree decreases. The bandwidth controls not only the amount of smoothing but also the optimal degree.

where $\beta_j = \langle Y, \psi_j \rangle$ are Fourier coefficients to be estimated. The coefficients can be estimated in the least squares method. Consider the triangular mesh for $\mathcal{M}$ consisting of n nodes. Denote

$$\mathbf{Y} = (Y(p_1), \cdots, Y(p_n))', \;\; \boldsymbol{\beta} = (\beta_0, \cdots, \beta_k)'.$$

Then, we can represent (14) as the normal equation,

$$\mathbf{Y} = \boldsymbol{\beta}\boldsymbol{\Psi}, \tag{15}$$

where $\boldsymbol{\Psi} = (\boldsymbol{\Psi}_0, \cdots, \boldsymbol{\Psi}_k)$ and $\boldsymbol{\Psi}_j = (\psi_j(p_1), \cdots, \psi_j(p_n))'$. The coefficients $\boldsymbol{\beta}$ are estimated in the least squares fashion [36] as

$$\widehat{\boldsymbol{\beta}} = (\boldsymbol{\Psi}'\boldsymbol{\Psi})^{-1}\boldsymbol{\Psi}'\mathbf{Y}. \tag{16}$$

Since the size of matrix $\boldsymbol{\Psi}'\boldsymbol{\Psi}$, i.e. $k \times k$, can become fairly large for large number of basis, it may be difficult to directly invert it when there is a need to obtain large number of basis. So we have adopted a more general iterative strategy to overcome the possible computational bottleneck by

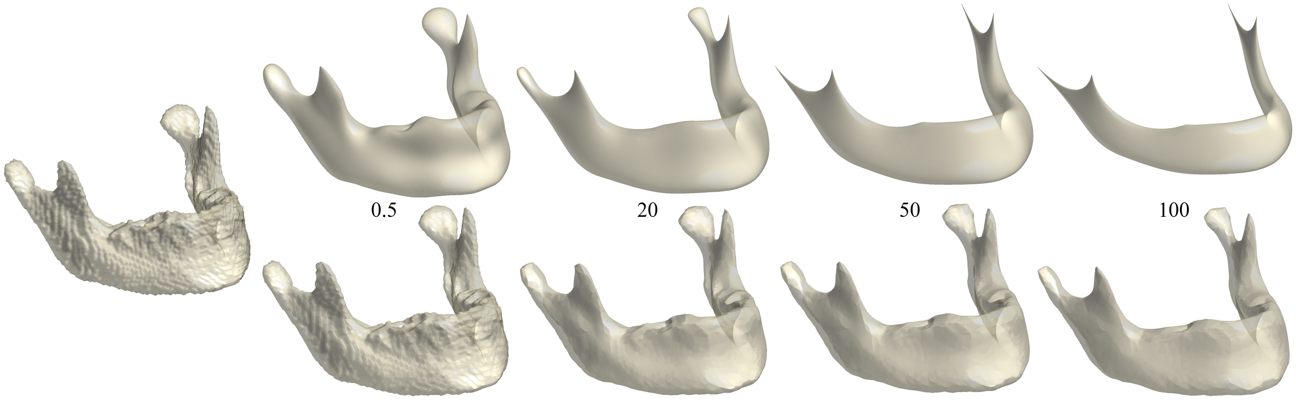

Figure 5: Smoothed mandible surfaces. Left: the original sample surface. Top: heat kernel smoothing with various bandwidths, $\sigma = 0.5, 20, 50$ and 100 which have corresponding optimal degrees, 132, 81, 30, and 24 respectively. Bottom: iterated kernel smoothing with fixed bandwidth $\sigma = 0.5/13$ with the varying number of iterations ($m = 13, 520, 1300$ and 2600), which results in the effective bandwidths $\sigma = 0.5, 20, 50$ and 100. The iterated kernel smoothing results are significantly different from the heat kernel smoothing results.

breaking a large least squares problem into smaller least squares problem using the *iterative residual fitting (IRF) algorithm* [37, 38] that was originally developed for spherical harmonic representation. In this paper, it will be shown that approximately 132 basis are sufficient for representing mandible surfaces making the direct matrix inversion possible without the use of the IRF-algorithm. However, we wanted to develop a more general framework that can be applied to complex high resolution surfaces like human brain surfaces.

The Fourier coefficients are estimated based on an iterative procedure that utilizes the orthonormality of the eigenfunctions. Decompose the subspace $\mathcal{H}_k$ into smaller subspaces as the direct sum

$$\mathcal{H}_k = \mathcal{I}_0 \oplus \mathcal{I}_1 \cdots \oplus \mathcal{I}_k,$$

where each subspace $\mathcal{I}_j$ is the projection of $\mathcal{H}_k$ along the j-th eigenfunction. Instead of directly solving the normal equation (15), we project the normal equations into a smaller subspace $\mathcal{I}_j$ and find the corresponding coefficient β_j in an iterative fashion from increasing the degree from 0 to k.

At degree $k = 0$, we write $\mathbf{Y} = \mathbf{\Psi}_0\beta_0 + \mathbf{r}_0$, where $\mathbf{r}_0$ is the residual of estimating $\mathbf{Y}$ in subspace

$\mathcal{I}_0$. Then, we estimate β_0 by minimizing the residual in the least squares fashion:

$$\widehat{\beta}_0 = (\mathbf{\Psi}_0'\mathbf{\Psi}_0)^{-1}\mathbf{\Psi}_0'\mathbf{Y} = \frac{\sum_{i=1}^n Y(p_i)\psi_0(p_i)}{\sum_{i=1}^n \psi_0^2(p_i)}. \tag{17}$$

At degree j, we have

$$\mathbf{r}_j = \mathbf{r}_{j-1} - e^{-\lambda_j \sigma}\mathbf{\Psi}_j\beta_j, \tag{18}$$

where the previous residual $\mathbf{r}_{j-1}$ is given by

$$\mathbf{r}_{j-1} = \mathbf{Y} - \sum_{i=0}^{j-1} e^{-\lambda_i \sigma}\mathbf{\Psi}_i\widehat{\beta}_i.$$

The parameter β_j is then estimated by minimizing the next residual $\mathbf{r}_j$ in the least squares fashion

$$\widehat{\beta}_j = (\mathbf{\Psi}_j'\mathbf{\Psi}_j)^{-1}\mathbf{\Psi}_j'\mathbf{r}_{j-1}.$$

The optimal stopping rule for the algorithm is determined if the decrease of the root mean squared errors (RMSE) is statistically no longer significant using the F-test [37, 38, 39]. Fig. 3 shows the the plot of RMSE that flattens out after certain degree. Once we estimated coefficients up to degree $k-1$, we test if adding the degree k term is statistically significant by testing the null hypothesis

$$H_0 : \widehat{\beta}_k = 0. \tag{19}$$

Let the *sum of squared errors* (SSE) of the k-th degree expansion be

$$\text{SSE}_k = \sum_{i=1}^n \Big[Y(p_i) - \sum_{j=0}^k e^{-\lambda_j \sigma}\widehat{\beta}_j\psi_j(p_i)\Big]^2. \tag{20}$$

RMSE is then given as $\sqrt{\text{SSE}_k/n}$. As the degree k increases, SSE_k decreases so it is reasonable to choose the k-th series expansion as optimal representation when the decrease of SSE_k is no longer significant. Under H_0, the test statistic F follows

$$F = \frac{\text{SSE}_{k-1} - \text{SSE}_k}{\text{SSE}_{k-1}/(n-k-2)} \sim F_{1,n-k-2}, \tag{21}$$

the F-distribution with 1 and $n-k-2$ degrees of freedom. We compute the F statistic at each degree, and find the degree of expansion where corresponding p-value first becomes bigger than the pre-specified significance $\alpha = 0.01$.

4 Experimental Results

We applied the proposed smoothing method to mandible surfaces obtained from CT. The method is further validated against the spherical harmonics on a unit sphere, and compared against iterative kernel smoothing methods [12, 13, 14].

4.1 Image Acquisition and Preprocessing.

The CT images used in the study were obtained using several different models of GE multi-slice helical CT scanners. The CT scans were acquired directly in the axial plane with a 1.25 mm slice thickness, matrix size of 512×512 and 15–30 cm field of view (FOV). Image resolution varied and was in the range of 0.29 to 0.59 mm as determined by the ratio of FOV divided by the matrix. CT scans were converted to DICOM format and subsequently Analyze 8.1 software package (AnalyzeDirect, Inc., Overland Park, KS) was used in segmenting binary mandible structure based on histogram thresholding. By checking the Euler characteristic, bone pores (holes) in mandible images were automatically filled up using morphological operations to make the mandible binary volume to be topologically equivalent to a solid sphere.

4.2 Results.

We applied the proposed method in smoothing a mandible surface. The optimal eigenfunction expansion was determined using the F-test at $\alpha = 0.01$. Since there are three different degrees corresponding to three coordinate functions, we choose the maximum of 3 optimal degrees as the overall optimal degree. Fig. 3 shows the plot of the RMSE of a mandible surface for varying degrees between 5 to 200. As the degree k increases, the RMSE for each coordinate rapidly decreases and starts to flatten out at a certain degree. The optimal degree for the sample surface is determined as 132 for bandwidth 0.5. As the bandwidth increases, the optimal degree decreases due to smoothing effect (Fig. 4). Fig. 5 shows the result of heat kernel smoothing. Since the optimal degree for one surface may not be optimal for other surfaces, we have computed the optimal degree for 9 more mandible surfaces and averaged them (Fig. 4). The optimal degrees at different bandwidths are $k = 185$ $(\sigma = 0.5)$, $k = 95$ $(\sigma = 20)$, $k = 42$ $(\sigma = 50)$, and $k = 29$ $(\sigma = 100)$. These values can be used as a guideline for determining approximate optimal degrees for other mandible surfaces.

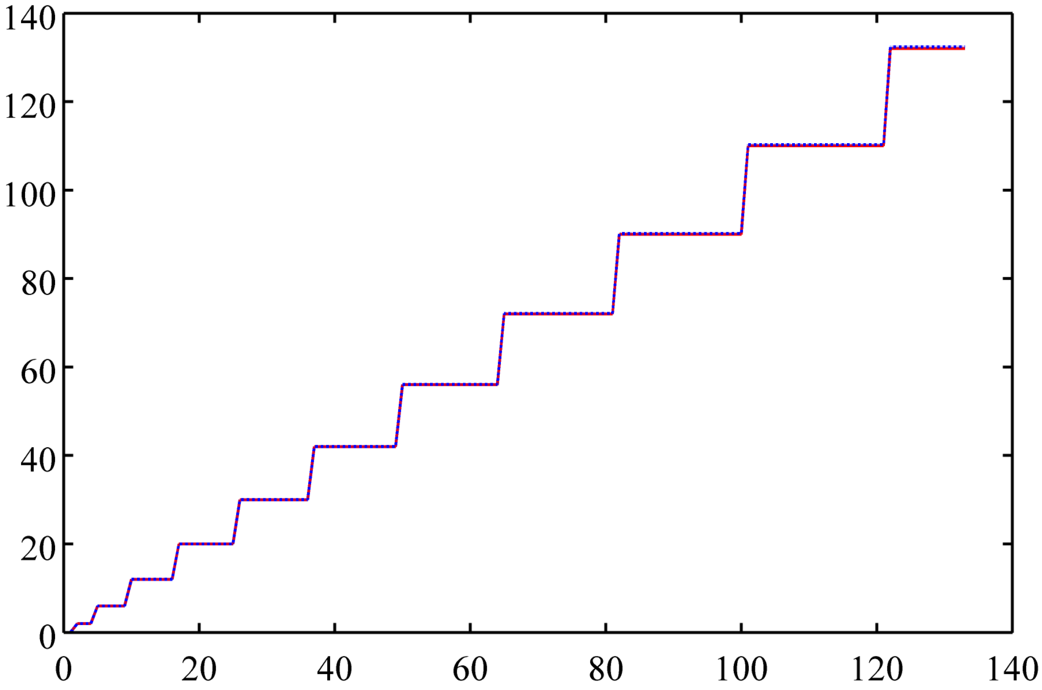

Figure 6: Comparison of eigenvalues for a unit sphere. 133 eigenvalues are numerically computed (blue dotted) and compared against the ground truth (red solid) $\lambda_l = l(l+1)$ for up to degree $l = 11$. They mach extremely well and the maximum possible relative error is 0.0032 (0.32%).

The numerical implementation was done with MATLAB 7.9 in 2 × 2.66 GHz Quad-Core Intel Xeon processor MAC PRO desktop with 32 GB memory. For the sample mesh with 22050 vertices, the entire process took approximately 75 seconds: 55 seconds for setting up the generalized eigenvalue problem (13), 10 seconds to actually solve it (13), 0.1 seconds for the IRF algorithm, and 9 seconds for finding the optimal degree.

4.3 Validation.

The proposed method is validated on a unit sphere where the ground truth is known. On the unit sphere, the Laplace-Beltrami eigenfunctions are spherical harmonics; however, due to the multiplicity of eigenvalues on the sphere, any linear combination of spherical harmonics of the same degree is again an eigenfunction. Therefore, we only checked if solving (13) produces the expected eigenvalues. We further checked if the constructed heat kernel matches to the ground

Table 1: Accuracy of eigenvalues.

Computed results		Theoretical values		
degree j	λ_j	degree l	order m	λ_l
0	0	0	0	0
1	2.0002	1	-1	2
2	2.0002	1	0	2
3	2.0002	1	1	2
4	6.0011	2	-2	6
9	12.0038	3	-3	12
16	20.0100	4	-4	20
25	30.0206	5	-5	30

truth on the unit sphere.

The parametrization of the unit sphere is given by

$$p = (\sin\theta\cos\varphi, \sin\theta\sin\varphi, \cos\theta),$$

with $(\theta, \varphi) \in [0, \pi] \otimes [0, 2\pi)$. The polar angle θ is the angle from the north pole and the azimutal angle φ is the angle along the horizontal cross-section. The spherical harmonic of degree l and order m, Y_{lm} [40, 41] is defined as

$$Y_{lm} = \begin{cases} c_{lm} P_l^{|m|}(\cos\theta)\sin(|m|\varphi), & -l \le m \le -1, \\ \frac{c_{lm}}{\sqrt{2}} P_l^{|m|}(\cos\theta), & m = 0, \\ c_{lm} P_l^{|m|}(\cos\theta)\cos(|m|\varphi), & 1 \le m \le l, \end{cases}$$

where $c_{lm} = \sqrt{\frac{2l+1}{2\pi}\frac{(l-|m|))!}{(l+|m|))!}}$ and P_l^m is the associated Legendre polynomials of order m given by

$$P_l^m(x) = \frac{(1-x^2)^{m/2}}{2^l l!}\frac{d^{l+m}}{dx^{l+m}}(x^2-1)^l, \ x \in [-1, 1].$$

There are $2l+1$ eigenfunctions Y_{lm} corresponding to the same eigenvalue $\lambda_l = l(l+1)$. Heat kernel is defined as

$$K_\sigma(p, q) = \sum_{l=0}^{\infty}\sum_{m=-l}^{l} e^{-l(l+1)\sigma} Y_{lm}(p) Y_{lm}(q), \tag{22}$$

while heat kernel smoothing of functional data Y is given by

$$K_\sigma * Y(p) = \sum_{l=0}^{\infty} \sum_{m=-l}^{l} e^{-l(l+1)\sigma} \beta_{lm} Y_{lm}(p), \tag{23}$$

where $p = (\theta, \varphi)$ and $\beta_{lm} = \langle Y, Y_{lm} \rangle$. The exact analytic form (22) serves as the ground truth for validation.

For validation, we computed eigenvalues and constructed the heat kernels on the spherical mesh with uniformly sampled 40,962 vertices. The validation is done two different ways.

(i) We investigated the accuracy of eigenvalues. Fig. 6 shows the 133 computed eigenvalues compared against the ground truth. The maximum possible relative error is 0.0032 (0.32%). Table 1 shows the numerical result for few selected eigenvalues.

(ii) To investigate the accuracy of the constructed heat kernel, we compared our method to the closed form (22). For our own method, we used expansion up to degree 132 while for (22), degree $l = 11$ was used. Fig. 7 shows the result of RMSE of proposed heat kernel smoothing against the ground truth. For sufficiently large bandwidth σ, RMSE is negligible.

4.4 Comparison.

The proposed heat kernel smoothing was compared against widely used iterated kernel smoothing [12, 14]. We have used the MATLAB implementation given in `http://www.stat.wisc.edu/~mchung/softwares/hk/hk.html`. In iterated kernel smoothing, the weights of the kernel are spatially adapted to follow the shape of heat kernel in discrete fashion along a surface mesh. Smoothing with large bandwidth is broken into iterated smoothing with smaller bandwidths:

$$K_{m\sigma} * Y = \underbrace{K_\sigma * \cdots * K_\sigma}_{m \text{ times}} * Y. \tag{24}$$

Denote the m-iterated kernel smoothing using a superscript as

$$K_\sigma^{(m)} * Y = \underbrace{K_\sigma * \cdots * K_\sigma}_{m \text{ times}} * Y.$$

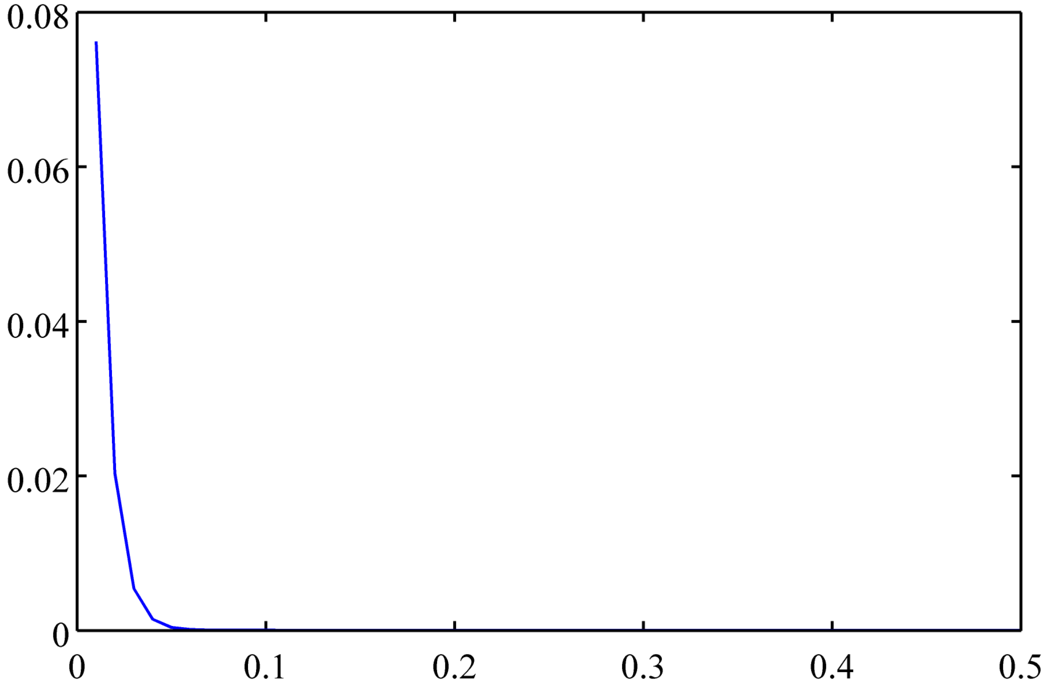

Figure 7: The plot of the root mean squared errors (RMSE) of constructed heat kernel against the ground truth on a unit sphere for varying bandwidth σ from 0.01 to 0.5. For sufficiently large bandwidth σ, RMSE is negligible.

Then using the *parametrix expansion* [25, 42], we approximated heat kernel locally using the Gaussian kernel for small bandwidth:

$$K_\sigma(p,q) = \frac{1}{\sqrt{4\pi\sigma}} \exp[-\frac{d^2(p,q)}{4\sigma}][1+O(\sigma^2)], \tag{25}$$

where $d(p,q)$ is the geodesic distance between p and q. For sufficiently small bandwidth σ, all the kernel weights were concentrated near the center, so the first neighbors of a given mesh vertex is sufficient for approximation. Unfortunately, this approximation is bound to compound error at each additional iteration. For numerical implementation, we used the normalized truncated kernel given by

$$\widetilde{W}_\sigma(p,q_i) = \frac{\exp\big[-\frac{d^2(p,q_i)}{4\sigma}\big]}{\sum_{j=0}^r \exp\big[-\frac{d^2(p,q_j)}{4\sigma}\big]}, \tag{26}$$

where $q_1, \cdots, q_r$ are r neighboring vertices of $p = q_0$. The discrete version of the iterated heat kernel smoothing is then defined as

$$\widetilde{W}_\sigma * Y(p) = \sum_{i=0}^r \widetilde{W}_\sigma(p,q_i) Y(q_i). \tag{27}$$

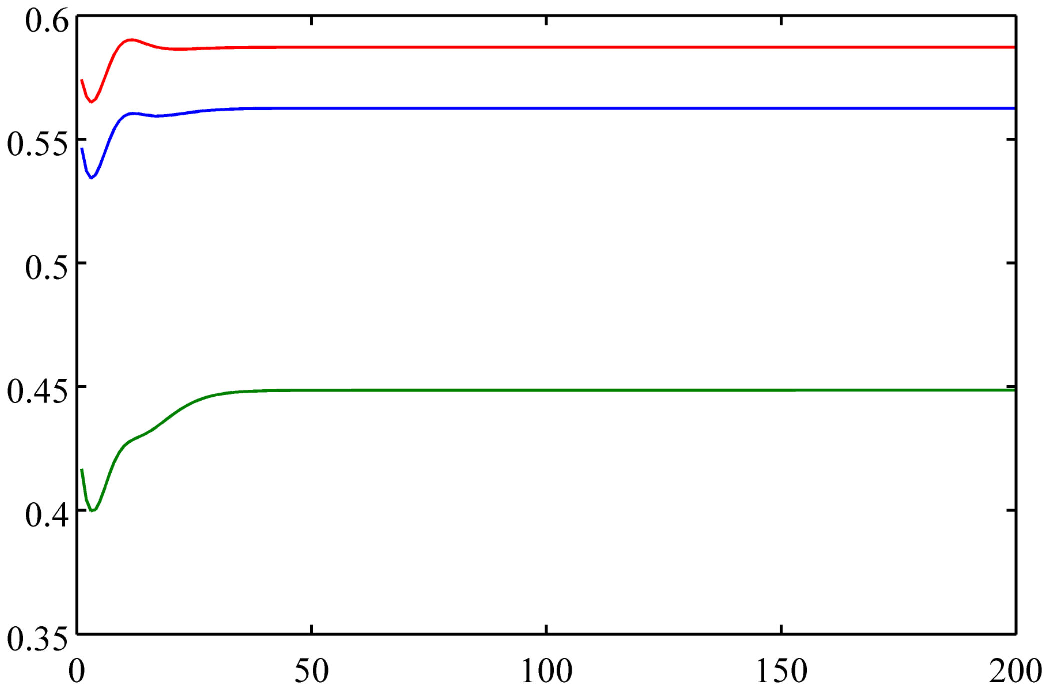

Figure 8: Plot of the RMSE of iterated kernel smoothing against the ground truth for coordinates x (blue), y (red) and z (green) over the number of iterations up to 200. The proposed heat kernel smoothing with $\sigma = 0.5$ and $k = 132$ is taken as the ground truth and iterative kernel smoothing is compared.

We compared the performance of iterated kernel smoothing (27) against heat kernel smoothing. Due to the lack of the ground truth on an arbitrary surface, there have been no validation framework on the performance of iterated kernel smoothing except [22]. For heat kernel smoothing, we used the bandwidth $\sigma = 0.5$ and eigenfunctions up to $k = 132$ degree. For iterated kernel smoothing, we varied the number of iterations $1 \leq m \leq 200$ with the correspondingly smaller bandwidth $0.5/m$ to have the effective bandwidth of 0.5. For the comparison of performance between both smoothing methods, we calculated RMSE. The performance of the iterated kernel smoothing depended on the number of iterations, as shown in the plot of RMSE of mesh coordinates over the number of iterations (Fig. 8). The RMSE was up to 0.5901 and it did not decrease even when we increase the number of iterations. This comparison quantitatively demonstrates the limitation of iterated heat kernel smoothing which does not converge to heat diffusion, and it is also visually demonstrated in Fig. 5.

In another comparison (Fig. 9), we numerically constructed a heat kernel with small bandwidth

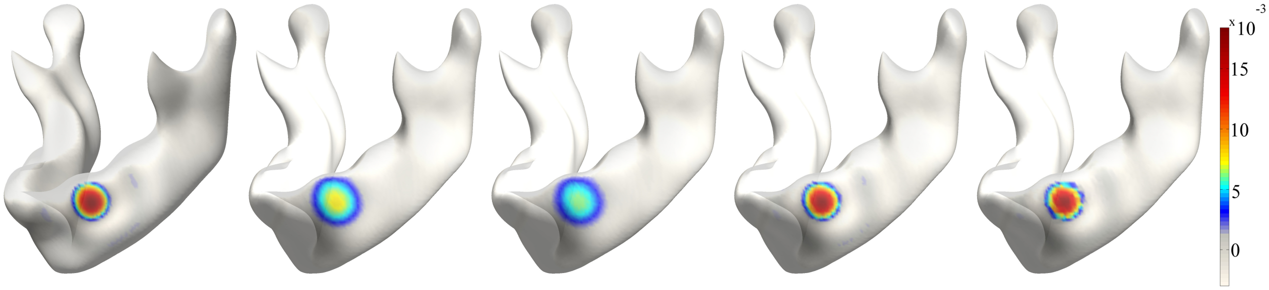

Figure 9: Kernel shape comparison. Heat kernel with bandwidth 0.025 is numerically constructed to be used as a sample data (1st). The sample data is smoothed using heat kernel smoothing with degree 132 and with bandwidth 1.225 (2nd) and 4.975 (3rd) resulting in the effective smoothing bandwidth of 1.25 and 5 respectively. Iterated kernel smoothing with bandwidth 0.025 is also applied to the sample data (1st) with 49 (4th) and 199 (5th) iterations to have the effective bandwidth of 1.25 and 5.

0.025 as a sample data. Then we performed the additional iterated kernel smoothing 49 and 199 times on the sample data to obtain a kernel with the effective smoothing bandwidth of 1.25 and 5. We also performed heat kernel smoothing on the sample data with degree 132 and bandwidths 1.225 and 4.975 making the effective bandwidths of 1.25 and 5 respectively. Fig. 9 displays the shape difference of the two kernels. The first three are from heat kernel smoothing and the last two are from iterated kernel smoothing. This visually demonstrates iterated kernel smoothing differs from heat kernel smoothing.

5 Conclusion

We presented a novel heat kernel smoothing framework where the smoothed data is expanded using the Laplace-Beltrami eigenfunctions analytically. The expansion is the solution of isotropic heat diffusion. The method was validated on a unit sphere, where heat kernel was given exactly in terms of spherical harmonics. As demonstrated in the validation, the proposed method is highly accurate making heat kernel smoothing the possible ground truth for comparing other smoothing techniques. Therefore, we have determined the accuracy of widely used iterated kernel smoothing which has not been properly validated yet due to the lack of the ground truth. Heat kernel smoothing outperforms iterated kernel smoothing in accuracy.

Acknowledgment

This work was supported by NIH Research Grant R01 DC6282 (MRI and CT Studies of the Developing Vocal Tract), from the National Institute of Deafness and other Communicative Disorders (NIDCD). Also, by a core grant P-30 HD03352 to the Waisman Center from the National Institute of Child Health and Human Development (NICHHD). WCU grant from the government of Korea to the Department of Brain and Cognitive Sciences, Seoul National University is also acknowledged. We thank Dongjun Chung, Lindell R. Gentry, Mike S. Schimek, Katelyn J. Kassulke and Reid B. Durtschi for assistance with image acquisition and image segmentation.

References

[1] P. Perona and J. Malik, "Scale-space and edge detection using anisotropic diffusion," *IEEE Trans. Pattern Analysis and Machine Intelligence*, vol. 12, pp. 629–639, 1990.

[2] A. Andrade, F. Kherif, J. Mangin, K. Worsley, A. Paradis, O. Simon, S. Dehaene, D. Le Bihan, and J.-B. Poline, "Detection of fmri activation using cortical surface mapping," *Human Brain Mapping*, vol. 12, pp. 79–93, 2001.

[3] M. Chung, "Statistical morphometry in neuroanatomy," Ph.D. Thesis., McGill University, 2001.

[4] A. Joshi, D. W. Shattuck, P. M. Thompson, and R. M. Leahy, "A parameterization-based numerical method for isotropic and anisotropic diffusion smoothing on non-flat surfaces," *IEEE Transactions on Image Processing*, vol. 18, no. 6, pp. 1358–1365, 2009.

[5] N. Sochen, R. Kimmel, and R. Malladi, "A general framework for low level vision," *IEEE Transactions on Image Processing*, vol. 7, pp. 310–318, 1998.

[6] R. Malladi and I. Ravve, "Fast difference schemes for edge enhancing beltrami flow," in *Proceedings of Computer Vision-ECCV*, 2002, pp. Part I 343–357.

[7] B. Tang, G. Sapiro, and V. Caselles, "Direction diffusion," in *The Proceedings of the Seventh IEEE International Conference on Computer Vision*, 1999, pp. 2:1245–1252.

[8] G. Taubin, "Geometric signal processing on polygonal meshes," in *Eurographics State of the Art Report*, 2000.

[9] M. Chung, K. Worsley, S. Robbins, T. Paus, J. Taylor, J. Giedd, J. Rapoport, and A. Evans, "Deformation-based surface morphometry applied to gray matter deformation," *NeuroImage*, vol. 18, pp. 198–213, 2003.

[10] A. Cachia, J.-F. Mangin, D. Riviere, F. Kherif, N. Boddaert, A. Andrade, D. Papadopoulos-Orfanos, J.-B. Poline, I. Bloch, M. Zilbovicius, P. Sonigo, F. Brunelle, and J. . Regis, "A primal sketch of the cortex mean curvature: a morphogenesis based approach to study the variability of the folding patterns," *IEEE Transactions on Medical Imaging*, vol. 22, pp. 754–765, 2003.

[11] A. Cachia, J.-F. Mangin, D. Riviére, D. Papadopoulos-Orfanos, F. Kherif, I. Bloch, and J. Régis, "A generic framework for parcellation of the cortical surface into gyri using geodesic voronoï diagrams," *Image Analysis*, vol. 7, pp. 403–416, 2003.

[12] M. Chung, S. Robbins, K. Dalton, R. Davidson, A. Alexander, and A. Evans, "Cortical thickness analysis in autism with heat kernel smoothing," *NeuroImage*, vol. 25, pp. 1256–1265, 2005.

[13] M. Chung, S. Robbins, and A. Evans, "Unified statistical approach to cortical thickness analysis," in *Information Processing in Medical Imaging (IPMI).* Springer, pp. 627–638.

[14] X. Han, J. Jovicich, D. Salat, A. van der Kouwe, B. Quinn, S. Czanner, E. Busa, J. Pacheco, M. Albert, R. Killiany *et al.*, "Reliability of MRI-derived measurements of human cerebral cortical thickness: the effects of field strength, scanner upgrade and manufacturer," *Neuroimage*, vol. 32, pp. 180–194, 2006.

[15] E. Luders, Thompson, P.M., K. Narr, A. Toga, L. Jancke, and C. Gaser, "A curvature-based approach to estimate local gyrification on the cortical surface," *NeuroImage*, vol. 29, pp. 1224–1230, 2006.

[16] C. Gaser, E. Luders, P. Thompson, A. Lee, R. Dutton, J. Geaga, K. Hayashi, U. Bellugi, A. Galaburda, J. Korenberg, D. Mills, A. Toga, and A. Reiss, "Increased local gyrification mapped in williams syndrome," *NeuroImage*, vol. 33, pp. 46–54, 2006.

[17] E. Luders, K. Narr, P. Thompson, D. Rex, R. Woods, and J. L. a. A. DeLuca, H., "Gender effects on cortical thickness and the influence of scaling," *Human Brain Mapping*, vol. 27, pp. 314–324, 2006.

[18] J. Bernal-Rusiel, M. Atienza, and J. Cantero, "Detection of focal changes in human cortical thickness: spherical wavelets versus gaussian smoothing," *NeuroImage*, vol. 41, pp. 1278–1292, 2008.

[19] L. Shen, A. Saykin, M. Chung, H. Huang, J. Ford, F. Makedon, T. McHugh, and C. Rhodes, "Morphometric analysis of genetic variation in hippocampal shape in mild cognitive impairment: Role of an il-6 promoter polymorphism," in *Life Science Society Computational Systems Bioinformatics Conference*, 2006.

[20] H. Zhu, J. Ibrahim, N. Tang, D. Rowe, X. Hao, R. Bansal, and B. Peterson, "A statistical analysis of brain morphology using wild bootstrapping," *IEEE Transactions on Medical Imaging*, vol. 26, pp. 954–966, 2007.

[21] J. Han, J. Kim, C. Chung, and K. Park, "Evaluation of smoothing in an iterative lp-norm minimization algorithm for surface-based source localization of meg," *Physics in Medicine and Biology*, vol. 52, pp. 4791–4803, 2007.

[22] D. Hagler Jr., A. Saygin, and M. Sereno, "Smoothing and cluster thresholding for cortical surface-based group analysis of fmri data," *NeuroImage*, vol. 33, pp. 1093–1103, 2006.

[23] H. Jo, J.-M. Lee, J.-H. Kim, Y.-W. Shin, I.-Y. Kim, J. Kwon, and S. Kim, "Spatial accuracy of fmri activation influenced by volume- and surface-based spatial smoothing techniques," *NeuroImage*, vol. 34, pp. 550–564, 2007.

[24] T. Tasdizen, R. Whitaker, P. Burchard, and S. Osher, "Geometric surface smoothing via anisotropic diffusion of normals," in *Geometric Modeling and Processing*, 2006, pp. 687–693.

[25] S. Rosenberg, *The Laplacian on a Riemannian Manifold.* Cambridge University Press, 1997.

[26] Y. Shi, I. Dinov, and A. Toga, "Cortical shape analysis in the Laplace-Beltrami Feature Space," in *Medical Image Computing and Computer-Assisted Intervention MICCAI 2009*, vol. Lecture Notes in Computer Science 5762. Springer Berlin / Heidelberg, 2009, pp. 208–215.

[27] B. Lévy, "Laplace-Beltrami Eigenfunctions: Towards an Algorithm that Understands Geometry," in *IEEE International Conference on Shape Modeling and Applications.* IEEE, 2006, p. 13.

[28] M. Chung and J. Taylor, "Diffusion smoothing on brain surface via finite element method," in *Proceedings of IEEE International Symposium on Biomedical Imaging (ISBI)*, 2004.

[29] A. Qiu, D. Bitouk, and M. Miller, "Smooth functional and structural maps on the neocortex via orthonormal bases of the laplace-beltrami operator," *IEEE Transactions on Medical Imaging*, vol. 25, pp. 1296–1396, 2006.

[30] M. Sadiku, "A simple introduction to finite element analysis of electromagnetic problems," *IEEE Transactions on Education*, vol. 32, pp. 85–93, 1989.

[31] ——, *Numerical Techniques in Electromagnetics.* CRC Press, 1992.

[32] P. Silvester and R. Ferrari, *Finite Elements for Electrical Engineers.* Cambridge: Cambridge Univ. Press, 1983.

[33] V. Hernandez, J. E. Roman, A. Tomas, and V. Vidal, "A survey of software for sparse eigenvalue problems," Universidad Politécnica de Valencia, Tech. Rep. STR-6, 2006, available at http://www.grycap.upv.es/slepc.

[34] R. Lehoucq, D. Sorensen, and C. Yang, *ARPACK Users' Guide: Solution of Large-Scale Eigenvalue Problems with Implicitly Restarted Arnoldi Methods.* Philadelphia: SIAM Publications, 1998.

[35] M. Hoffmann-Ostenhof, T. Hoffmann-Ostenhof, and N. Nadirashvili, "On the Multiplicity of Eigenvalues of the Laplacian on Surfaces," *Annals of Global Analysis and Geometry*, vol. 17, 1999.

[36] M. Styner, I. Oguz, S. Xu, C. Brechbuhler, D. Pantazis, J. Levitt, M. Shenton, and G. Gerig, "Framework for the statistical shape analysis of brain structures using spharm-pdm," in *Insight Journal, Special Edition on the Open Science Workshop at MICCAI*, 2006, http://hdl.handle.net/1926/215.

[37] M. Chung, K. Dalton, L. Shen, A. Evans, and R. Davidson, "Weighted Fourier representation and its application to quantifying the amount of gray matter," *IEEE Transactions on Medical Imaging*, vol. 26, pp. 566–581, 2007.

[38] M. Chung, R. Hartley, K. Dalton, and R. Davidson, "Encoding cortical surface by spherical harmonics," *Satistica Sinica*, vol. 18, pp. 1269–1291, 2008.

[39] M. Chung, N. Adluru, J. Lee, M. Lazar, J. Lainhart, and A. Alexander, "Cosine series representation of 3d curves and its application to white matter fiber bundles in diffusion tensor imaging," *Statistics and Its Interface*, vol. 3, pp. 69–80, 2010.

[40] R. Courant and D. Hilbert., *Methods of Mathematical Physics, Volume I.* New York: Interscience, 1953.

[41] G. Wahba, *Spline models for observational data.* SIAM, 1990.

[42] F.-Y. Wang, “Sharp explict lower bounds of heat kernels,” *Annals of Probability*, vol. 24, pp. 1995–2006, 1997.